Full Length Article

Simple construction and reversible sequential evolution mechanism of nitrogen-doped mesoporous carbon/SnS$_2$ nanosheets in lithium-ion batteries

Kun Liu [a,1], Jia-ao Wang [b,1], Chenjie Lou [c], Ziru Zhou [d], Ning Zhang [a], Yingtao Yu [d], Qingxiao Zhang [e,**], Graeme Henkelman [b], Mingxue Tang [c], Juncai Sun [a,*]

[a] Institute of Materials and Technology, Dalian Maritime University, Dalian 116026, China
[b] Department of Chemistry and the Oden Institute for Computational Engineering and Sciences, The University of Texas at Austin, Austin, TX 78712-0165, USA
[c] Center for High Pressure Science & Technology Advanced Research, Beijing 100094, China
[d] College of Environmental Science and Engineering, Dalian Maritime University, Dalian 116026, China
[e] School of Chemistry and Chemical Engineering, Shandong University of Technology, Zibo 255049, China

ARTICLE INFO

ABSTRACT

Tin sulfide/nitrogen-doped mesoporous carbon (SnS$_2$/NC) composite material is identified as a prospective anode material in lithium-ion batteries. Nevertheless, the evolution mechanism of SnS$_2$/NC anode and the electronic conductivity of nitrogen-doped carbon to SnS$_2$ are still unclear. Meanwhile, the preparation process of SnS$_2$/NC is complicated and requires the use of harmful solvents. Herein, we propose a simple and green strategy for the construction of SnS$_2$/NC nanosheets, and investigate its evolution mechanism and electronic conductivity in detail. DFT calculations substantiate the improved electronic conductivity and heightened Li adsorption affinity after N doping. Profiting from the enhancement of electronic conductivity and Li adsorption affinity, the SnS$_2$/NC anode attains a satisfactory discharge capacity (863.9 mAh/g at 100 mA/g over 100 cycles). Correspondingly, the assembled full cell achieves a capacity attenuation of solely 0.3% per cycle over 90 cycles. Upon lithiation, a sequential evolution mechanism, containing intercalation, conversion and alloying reactions, is reported on the basis of in-situ XRD, ex-situ XPS, and NMR characterizations. Additionally, ex-situ Raman reveals the reversible evolution of SnS$_2$. These findings could afford significant reference and guideline for the evolution mechanism of other metal sulfides materials in energy storage areas.

1. Introduction

Two-dimensional (2D) layered metal dichalcogenides (e.g., FeS$_2$ [1], CoS$_2$ [2], MoS$_2$ [3], and SnS$_2$ [4]) have recently triggered remarkable attention in lithium-ion batteries (LIBs) due to their enchanting theoretical capacity and rich resources. Among these metal dichalcogenides, SnS$_2$ possessing a layered CdI$_2$-type structure is viewed as a hopeful anode material in LIBs because of its appealing theoretical specific capacity of 1232 mAh/g and large interlayer spacing of 5.9 Å [5,6]. Unfortunately, the electrochemical properties of SnS$_2$ electrode sharply fade upon cycling processes owing to its inferior conductivity and vast volume variation, which extremely restrains its practical applications

[7,8].

Preparation of composites of SnS$_2$ nanostructures and carbonaceous materials is the most popular applied method to circumvent these obstacles [9-12]. The nanostructured SnS$_2$ with various morphologies, such as nanoparticles [13], nanoflowers [14], nanorods [15], nanobelts [16], and nanosheets [17], could effectively dilute the mechanical stress caused by volume variation upon cycling and decrease the Li$^+$ diffusion path, leading to an enhanced rate performance [18,19]. In addition, the integration of carbonaceous materials into SnS$_2$ nanostructures could greatly ameliorate the conductivity and cushion the volume variation of the electrodes [20].

More impressively, heteroatom (N, S, B, P, etc.) doping has become a

---
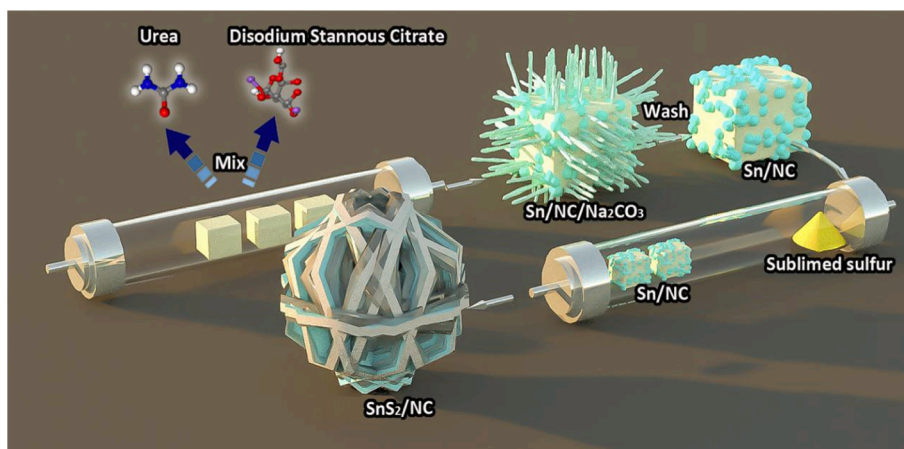
Scheme 1. Schematic diagram of SnS$_2$/NC synthesis.

valid tactic to fortify the physical and chemical properties of carbonaceous materials [21,22]. Specifically, N-doping in the carbonaceous material could heighten electrical conductivity, introduce defects, and generate more active sites for Li$^+$ storage [23,24]. Additionally, N-doped carbon (NC) can produce a stronger attraction to Li$^+$, thereby affording an improved rate capability [25]. Some researchers introduced N-doped carbon matrix (NCM) to augment the conductivity and cushion the volume variation, and improved Li$^+$ storage properties are realized in SnS$_2$/NC composite, such as the fabrication of SnO$_2$-SnS$_2$@C/NG [26], SnO$_2$@SnS$_2$@NG [27], HPC-SnS$_2$-PAN [28] and N-HPC/SnS$_2$ composites [24]. The better electrochemical performances of these composites are connected with the synergistic effect between nanostructures and NCM or N-carbon coating. Nevertheless, the advancement of SnS$_2$/NC anode is still in its infancy and there still remains some pivotal issues unresolved: i) the hydrothermal or solvothermal methods for the synthesis of SnS$_2$/NC composites were a complex multi-step procedure demanding long reaction times, high-cost Teflon-lined autoclave, and the use of harmful solvents, which hindered the mass production for commercialized application. ii) The affect of N-doping on electronic conductivity and Li$^+$ storage behaviors of SnS$_2$ was relatively ambiguous. iii) The electrochemical evolution mechanism of SnS$_2$ at different charge/discharge states was still unclear. Consequently, to fully tap the potential of SnS$_2$-based anode, designing a simple and green strategy to prepare SnS$_2$/NC composite and deeply comprehending its evolution mechanism and electronic conductivity of nitrogen-doped carbon to SnS$_2$ is extremely essential.

This work reports a facile and green strategy for the construction of SnS$_2$/NC nanosheets. DFT calculations reveal the improvement of electronic conductivity and adsorption affinities of Li after N doping. In view of these merits, the as-synthesized composite achieves remarkable electrochemical properties in half batteries and good application prospects in full batteries. Upon initial lithiation/de-lithiation, a reversible sequential evolution mechanism of lithium ion and SnS$_2$/NC is studied in detail based on in-situ XRD, ex-situ XPS, NMR, and Raman.

2. Experimental

2.1. Materials fabrication

2.1.1. Synthesis of Sn/N-doped mesoporous carbon (Sn/NC) and Sn/mesoporous carbon (Sn/C)

Sn/NC composite was synthesized through pyrolysis of a mixture of disodium stannous citrate (5 g) and urea (0.15 g) at 750 °C for 1 h under Ar protective environment and then cleaned the self-formed template (Na$_2$CO$_3$) with deionized (DI) water. The preparation of Sn/mesoporous carbon (Sn/C) composite was performed according to the same process except for the absence of urea.

2.1.2. Synthesis of SnS$_2$/NC and SnS$_2$/C

SnS$_2$/NC composite was obtained by a facile sulfuration process as follows: Two individual alumina square crucibles loading 0.4 g prepared Sn/NC and 2 g sublimed sulfur were successively placed in the tubular furnace, followed by heating to 500 °C for 3 h. Additionally, SnS$_2$/C composite was manufactured by applying the same procedure as SnS$_2$/NC.

2.2. Materials characterizations

Field-emission scanning electron microscope (FE-SEM, SUPER55/SAPPHIRE) and transmission electron microscopy (TEM, JEM-2100) were performed to discern the microstructural features. X-ray diffraction (XRD) patterns were recorded applying Rigaku-D/MAX-3A with Cu-Kα radiation (λ = 1.5406 Å). Raman spectra were gained through a T64000 triple Raman spectrometer. Fourier transform infrared (FTIR) spectroscopy was collected with Thermo Fisher Nicolet Is10. Thermogravimetric analysis (TGA) was fulfilled on NETZSCH-STA409C. N$_2$ adsorption and desorption isotherms were performed via a micromeritics ASAP 2020. X-ray photoelectron spectroscopy (XPS) was implemented using a Kratos Axis Ultra DLD. The electronic conductivities were determined applying a four-point probe (FT-341) method.

To comprehend the electrochemical reaction mechanism of SnS$_2$/NC electrode, in-situ XRD analysis was carried out on Shimadzu XRD-7000 diffractometer with Be window as the X-ray penetration. For ex-situ Raman and XPS measurements, the coin-type cells were dismantled in a glove box. The resulting pole pieces were cleaned in dimethyl carbonate solvent to remove the residual electrolyte and then dried in vacuum before the ex-situ characterizations.

All ^{6,7}Li Magic Angle Spinning Nuclear Magnetic Resonance (MAS NMR) experiments were acquired on Bruker 600 MHz (14.1 T) magnets with AVANCE NEO consoles using Bruker 3.2 mm HXY MAS probe. All samples were packed into rotors inside an Ar-filled glove box. The Larmor frequency for ^{6}Li and ^{7}Li were 88.30 and 233.18 MHz, respectively. All ^{6,7}Li were acquired by using single one-pulse program and referenced to 1 M LiCl solution at 0 ppm. The duration of the $\pi/2$ pulse was 2 μs for ^{6}Li and 4 μs for ^{7}Li, respectively. The spinning rate was set to 18 kHz.

2.3. Electrochemical tests

The electrodes were manufactured by mixing with active materials, carbon black and sodium carboxymethyl cellulose (7:2:1) in DI water. The coin cells (CR-2032) were assembled with Li foils as counter electrode in a glove box. The Celgard 2400 membrane and 1 M LiPF$_6$ dissolved in ethylene carbonate/dimethyl carbonate/diethyl carbonate (EC/DMC/DEC, v/v/v = 1:1:1) were successively applied as the separator and electrolyte. The loading mass and thickness of active material
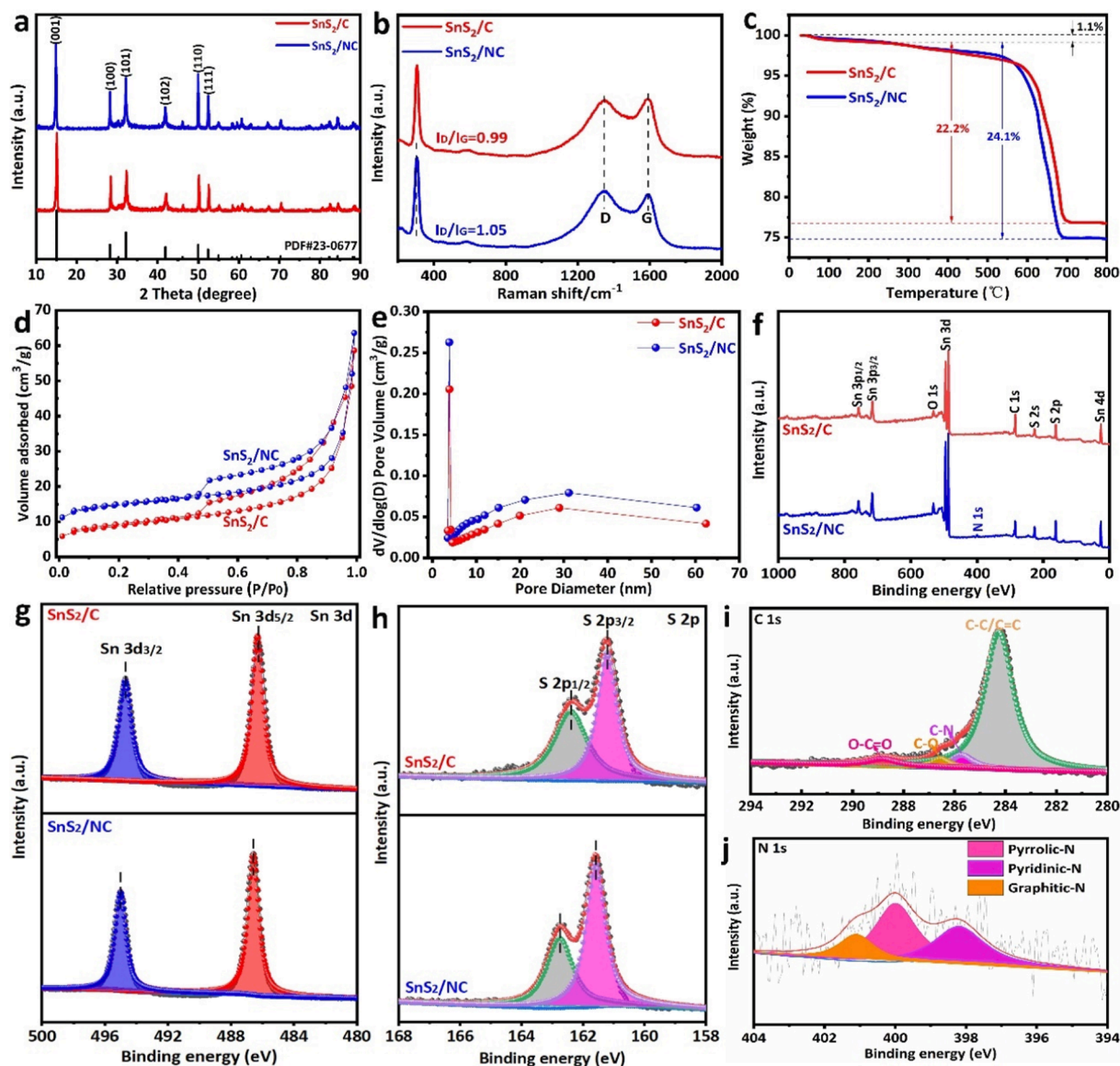
Fig. 1. Characterizations of SnS$_2$/NC and SnS$_2$/C: (a) XRD patterns, (b) Raman spectra, (c) TGA curves, (d) N$_2$ adsorption/desorption isotherms and (e) pore size distribution plots, (f) XPS full spectra, the magnified (g) Sn 3d, (h) S 2p, (i) C 1s and (j) N 1s spectrum.

in electrode were around 1.1–1.3 mg/cm^2 and 21 μm, separately. The galvanostatic charge/discharge (GCD) and galvanostatic intermittent titration technique (GITT) tests were executed on a LAND-CT2001A. CHI660D electrochemical workstation was utilized to test cyclic voltammetry (CV) and electrochemical impedance spectra (EIS).

The CR2032-type full cell was assembled via employing the as-prepared SnS$_2$/NC as anode and commercial LiCoO$_2$ as cathode. The charge/discharge performances of the full cell were tested at 200 mA/g between 2.0 and 3.9 V.

2.4. Computational details

Density functional theory (DFT) calculations were implemented by using Vienna Ab initio Simulation Package (VASP) [29,30]. The projector augmented wave (PAW) method and generalized gradient approximation (GGA) with the Perdew-Burke-Ernzerhof (PBE) function were separately adopted to portray the electron–ion interactions and electron exchange–correlation energy [11]. All the atoms were completely relaxed during the calculation. The geometry optimizations and self-consistent computations are built with the cutoff energy of 400

eV and a sampled Brillouin zone of 2 × 5 × 1 k-points model that accommodate the Monkhorst-Pack scheme grid mesh. The convergence criteria is projected with 0.02 eV/Å in force and 10^{-6} eV in energy.

3. Results and discussion

Scheme 1 depicts a schematic diagram of SnS$_2$/NC synthesis. After direct pyrolysis of the mixture, the obtained Na$_2$CO$_3$ template and Sn particles are dispersed within the carbon matrix (CM), which can be observed by SEM image (Fig. S1). The existence of Na$_2$CO$_3$ is also demonstrated via XRD (Fig. S2). After cleaning with DI water, the Na$_2$CO$_3$ is removed and Sn/NC sample is gained. The XRD (Fig. S3) and SEM (Fig. S4) further identify the formation of Sn/NC. Subsequently, through a facile sulfuration treatment using sublimed sulfur, the Sn/NC composite is successfully converted as SnS$_2$/NC.

The XRD was applied to confirm the crystal structure of SnS$_2$/NC and SnS$_2$/C. As plotted in Fig. 1a, the diffraction signature is well indexed to hexagonal SnS$_2$, exhibiting a high crystallinity. However, the diffraction signature of carbon hasn't been found because of the amorphous form. Raman spectra further supply details about the structural information
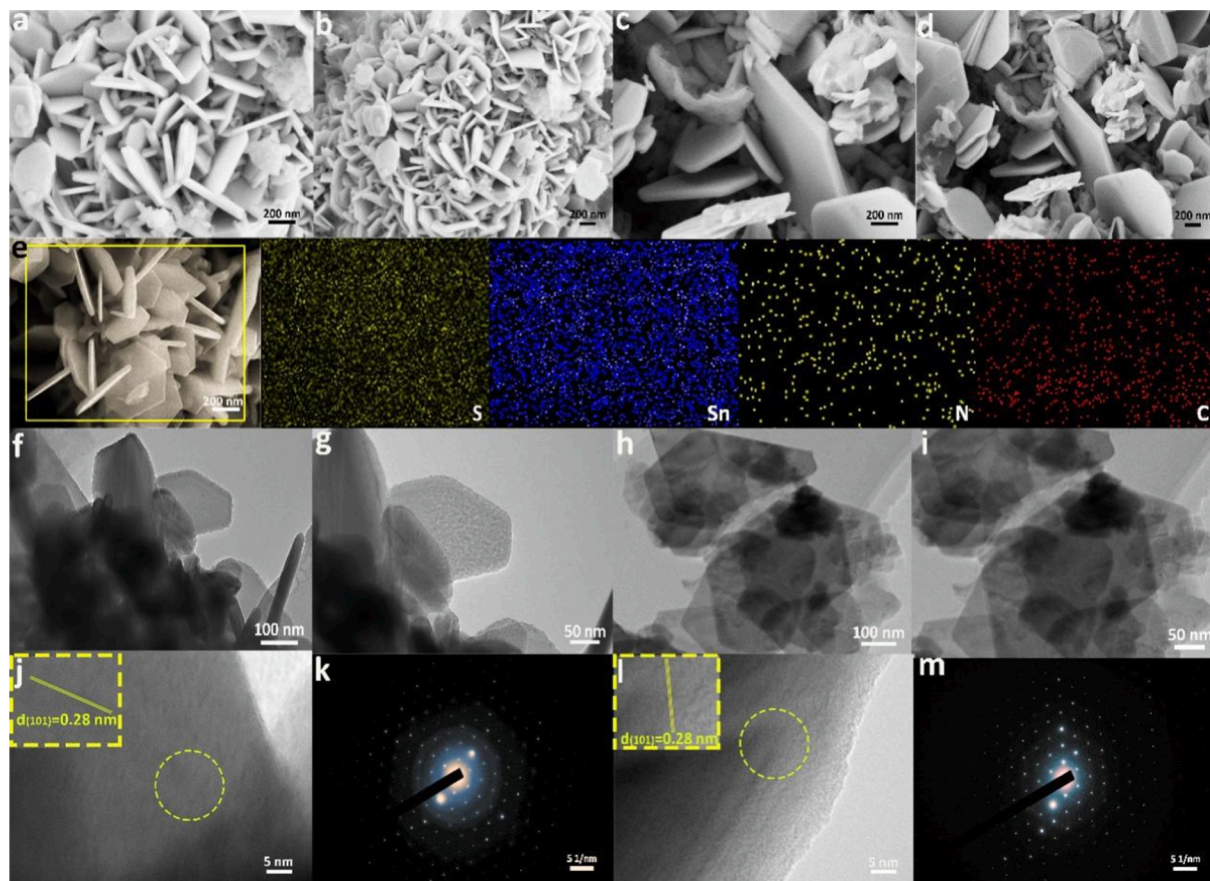
Fig. 2. SEM images of (a-b) SnS_2/NC and (c-d) SnS_2/C. (e) Elemental mapping of SnS_2/NC. TEM images of (f-g) SnS_2/NC and (h-i) SnS_2/C. (j) HR-TEM image and (k) SAED pattern of SnS_2/NC. (l) HR-TEM image and (m) SAED pattern of SnS_2/C.

(Fig. 1b). The narrow band (307 cm^{-1}) originates from the A_{1g} mode of SnS_2 in both SnS_2/NC and SnS_2/C, and another two wide peaks at 1345 and 1591 cm^{-1} are successively stemmed from defected-induced D band and graphitic G band of carbon [31]. This result reflects the coexistence of SnS_2 and carbon. The I_D/I_G value is generally utilized to reflect the defect degree in CM [24]. Relative to SnS_2/C sample (0.99), the I_D/I_G value in SnS_2/NC is 1.05, indicating that the defect degree is enhanced after N-doping. The chemical bonding of SnS_2/NC and SnS_2/C was characterized by FTIR (Fig. S5a). The band at 627 cm^{-1} is stemmed from Sn-S bond in both samples [32], suggesting that the SnS_2 is successfully prepared. Additionally, the band (1443 cm^{-1}) in SnS_2/NC is associated with the C-N bond, which illustrates the presence of the N element. TGA was operated for estimating the content of SnS_2 in SnS_2/NC and SnS_2/C. Below 250 °C, there is around 1.1% weight loss of absorbed water (Fig. 1c). The weight loss between 250 and 690 °C is related to the oxidation of SnS_2 to SnO_2 and the decomposition of carbon. Consequently, the content of SnS_2 in SnS_2/NC and SnS_2/C is determined to be around 91.7% and 94.1%, respectively. The BET results deliver that the specific surface areas (SSA) of SnS_2/NC and SnS_2/C reach 53.2 and 31.6 m^2/g, separately, (Fig. 1d), and their average pore diameters are about 12 nm based on the BJH desorption results, suggesting a mesoporous structure (Fig. 1e). The larger SSA and mesoporous structure of SnS_2/NC can serve as rapid channels for the transmission of Li$^+$.

Fig. 1f records the XPS spectra of SnS_2/NC and SnS_2/C. The S, Sn, O, and C elements are detected in SnS_2/NC and SnS_2/C. In comparison with SnS_2/C, SnS_2/NC has a peak of N 1s. It can be confirmed by Elemental Analyzer that the content of N in the SnS_2/NC is 0.99%. Fig. 1g gives the Sn 3d spectra, two peaks at 495 and 486.6 eV substantiate the formation of Sn^{4+} [32]. The S 2p spectra in Fig. 1h are deconvoluted as S 2p$_{3/2}$ (161.58 eV) and S 2p$_{1/2}$ (162.75 eV), conforming with the S^{2-} species

[7]. The above results demonstrate the successful formation of SnS_2 phase again. It can be found that the peaks of Sn 3d and S 2p for SnS_2/NC composite emerge a slightly shifted with respect to SnS_2/C, which may be caused by the interaction between SnS_2 and NC [27,33]. As observed in Fig. 1i, the C 1s spectrum of SnS_2/NC is split into four components (284.25 eV, 285.7 eV, 286.5 eV, and 288.8 eV) [13,27]. The formation of C-N verifies N doping into the CM. Specifically, the spectrum of N 1s (Fig. 1j) is fitted with three peaks at about 400 eV (Pyrrolic-N), 398.2 eV (Pyridinic), and 401.1 eV (Graphitic-N), individually [34]. Based on the area percentage of the N 1s peaks, the proportion of pyridinic-N, pyrrolic-N and graphitic-N was 34.1%, 47.2%, and 18.7%, separately (Fig. S5b). The NC is helpful for the enhancement of conductivity and the increment of defects, thus facilitating the electrochemical properties.

During the sulfuration process, Sn particles obtained (Fig. S4) by direct pyrolysis of disodium stannous citrate can grow unlimited and pierce the CM to turn into SnS_2 nanosheets. The morphologies of SnS_2/C and SnS_2/NC are identified by employing SEM and TEM images. It can be found from Fig. 2a-b that the SnS_2/NC composite is mainly constructed from highly ordered hexagonal nanosheets vertically arranged and compounded with NC, with 29–60 nm in thickness and 200–300 nm in diameter (Fig. 2f-g). A similar morphology is seen for the SnS_2/C composite prepared without N-doping (Fig. 2c-d). The EDS mappings (Fig. 2e) collected from the SnS_2/NC portray the distribution of Sn, S, N, and C elements.

The TEM images displayed in Fig. 2f-i reveal the nanosheet architecture of SnS_2 comprised of hexagons, which well supports the SEM observations. HR-TEM unveils that the interplanar distance of SnS_2/NC (Fig. 2j) and SnS_2/C (Fig. 2l) is both 0.28 nm, which stems from (1 0 1) plane of the SnS_2. The SAED patterns from Fig. 2k and m present a series of distinct diffraction spots, verifying that the SnS_2 is a monocrystalline
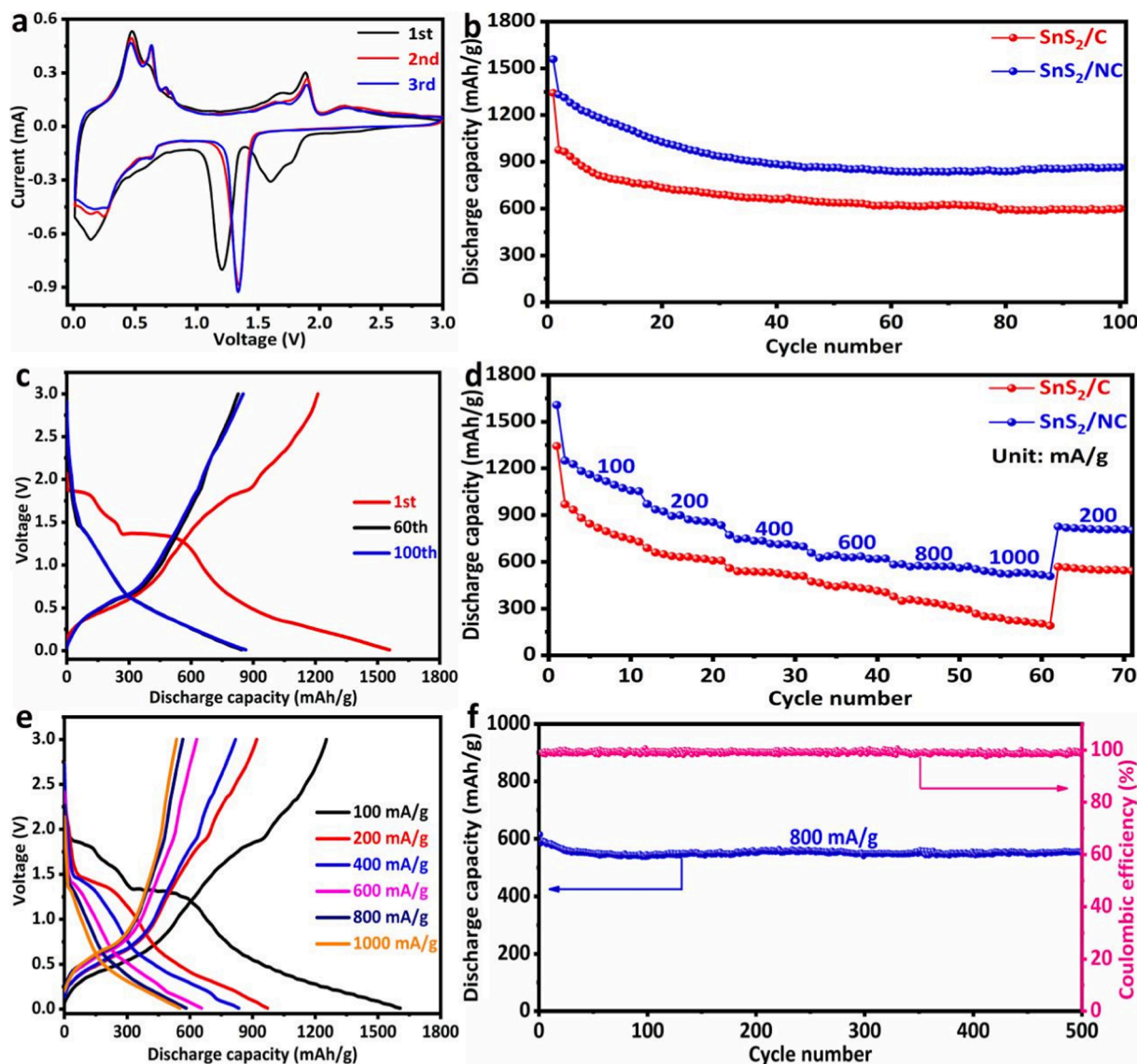
Fig. 3. (a) CV curves of SnS$_2$/NC at 0.1 mV/s. (b) Cyclic properties of SnS$_2$/NC and SnS$_2$/C at 100 mA/g. (c) GCD profiles of SnS$_2$/NC. (d) Rate capability of SnS$_2$/NC and SnS$_2$/C. (e) GCD profiles of SnS$_2$/NC from 100 to 1000 mA/g. (f) Cyclic property of SnS$_2$/NC at 800 mA/g.

feature [35,36].

Fig. 3a presents the initial three CV curves. During the 1st cathodic sweep, a peak at ~1.78 V originates from the Li$^+$ embedding into SnS$_2$ to form Li$_x$SnS$_2$ (Eq. (1)) [37,38]. The peaks at ~1.6 and ~1.21 V are connected with the decomposition of SnS$_2$ into metallic Sn and Li$_2$S (Eqs. (2) and (3)), and the generation of the SEI [17,20]. Additionally, a peak at ~0.14 V corresponds to the emergence of Li$_x$Sn alloy (Eq. (4)) [4]. During the 1st anodic sweep, the peaks emerged at 0.48–0.81 V derive from the dealloying process of Li$_x$Sn [28,39]. The two peaks at ~1.89 and ~2.2 V denote the extraction of Li$^+$ from Li$_x$SnS$_2$ and the conversion of unreacted Li$_2$S to polysulfides [17,40]. The CV profiles superimpose well during the following cycles, reflecting better reversibility. The CV profiles of SnS$_2$/C also present similar shape of peaks (Fig. S6). The above electrochemical conversion reactions are described in (1)-(4):

$$SnS_2 + xLi^+ + xe^- \rightarrow Li_xSnS_2 \tag{1}$$

$$Li_xSnS_2 + (4-x)Li^+ + (4-x)e^- \rightarrow Sn + 2Li_2S \tag{2}$$

$$SnS_2 + 4Li^+ + 4e^- \rightarrow Sn + 2Li_2S \tag{3}$$

$$Sn + yLi^+ + ye^- \rightarrow Li_ySn \tag{4}$$
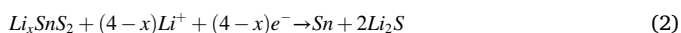
Fig. 3b gives the cyclic properties of SnS$_2$/NC and SnS$_2$/C. The SnS$_2$/NC electrode affords the discharge/charge capacities of 1558.1/1211.8 mAh/g (Fig. 3c), taking on an initial coulombic efficiency (ICE) of 77.8%, higher than SnS$_2$/C (71.5%, Fig. S7). Furthermore, the SnS$_2$/NC electrode yields a discharge capacity of 863.9 mAh/g over 100 cycles. Contrarily, the discharge capacity of the SnS$_2$/C only stabilizes around 599.6 mAh/g. Additionally, the rate properties of SnS$_2$/NC and SnS$_2$/C are recorded at different current densities (Fig. 3d). Notably, the rate capability of SnS$_2$/NC electrode is larger than SnS$_2$/C electrode. SnS$_2$/NC electrode renders a series of initial discharge capacities of 1694.9, 971.4, 834, 657.1, 582.6, and 553.1 mAh/g at 100, 200, 400, 600, 800, and 1000 mA/g in sequence (Fig. 3e). The properties are higher than SnS$_2$/C electrode (Fig. S8). After converting to 200 mA/g, the capacity of the SnS$_2$/NC electrode suddenly ascends up to 825.9 mAh/g. More than that, SnS$_2$/NC electrode achieves terrific cycling stability as well (Fig. 3f). The SnS$_2$/NC electrode still preserves well over 500 cycles, achieving a discharge capacity of 553.5 mAh/g, with a CE of approximately 99%.

In comparison to the previously reported SnS$_2$-based anodes, the SnS$_2$/NC electrode affords a satisfactory discharge capacity (Table S1). This is resulted from the synergism between SnS$_2$ nanosheets and NC,
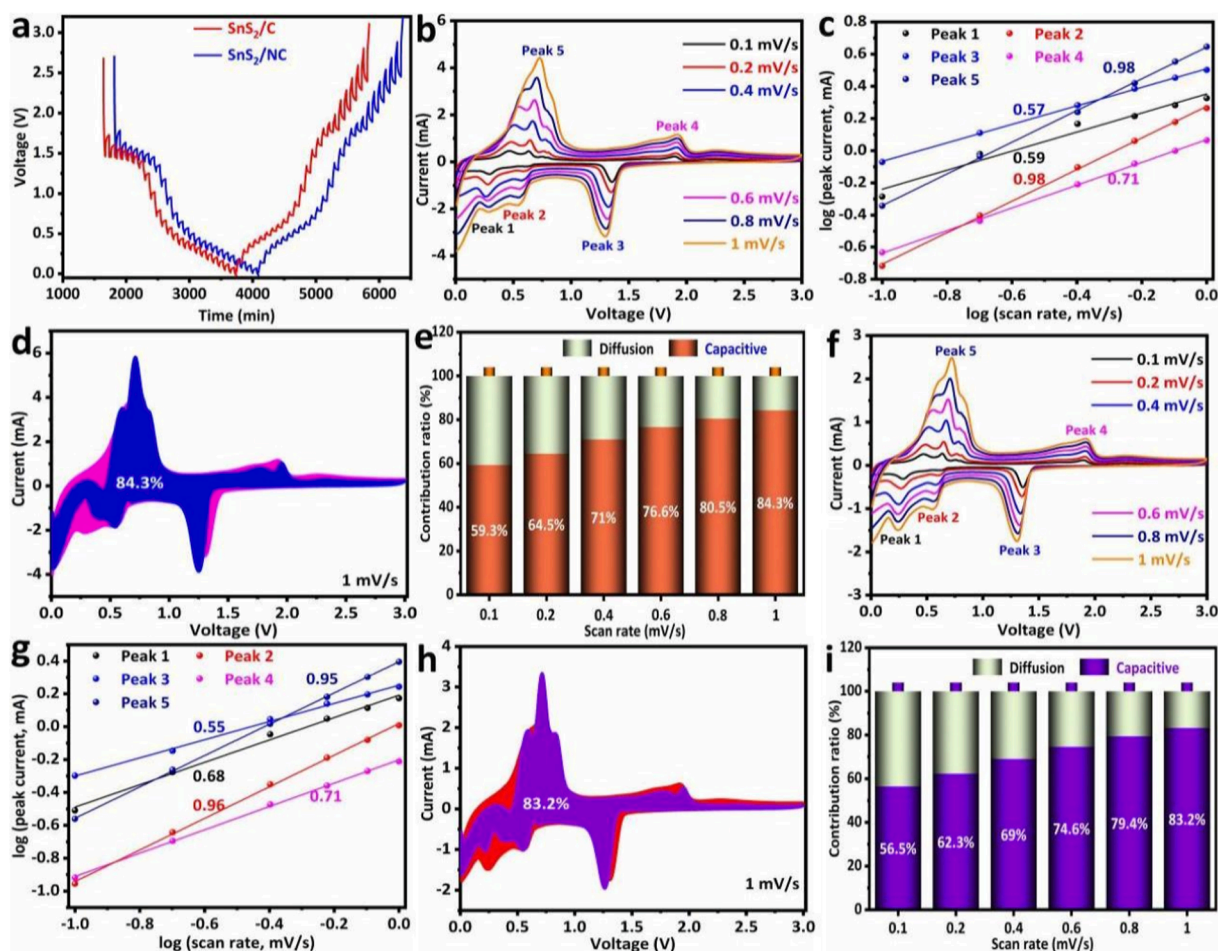
Fig. 4. (a) GITT profiles of SnS$_2$/NC and SnS$_2$/C. CV profiles of (b) SnS$_2$/NC and (f) SnS$_2$/C at various sweep rates. b-value analysis for (c) SnS$_2$/NC and (g) SnS$_2$/C. Capacitive contributions of (d) SnS$_2$/NC and (h) SnS$_2$/C. Contribution ratio of capacitive and diffusion-controlled for (e) SnS$_2$/NC and (i) SnS$_2$/C at various sweep rates.

remarkably elevating the lithium storage properties of SnS$_2$/NC. On the one hand, the NC could fortify the electronic conductivity of SnS$_2$. On the other hand, the N-doping could increase the defect in the CM and provide more active sites, promoting the diffusion of Li$^+$.

EIS tests were performed in Fig. S9 to monitor the electrochemical kinetics of SnS$_2$/NC and SnS$_2$/C. SnS$_2$/NC shows a smaller semicircle than SnS$_2$/C, attesting that the NC can fortify the electronic conductivity of the electrode, which is ulteriorly authenticated through four-point probe measurement (Fig. S10). The lithium reaction kinetics of SnS$_2$/NC and SnS$_2$/C electrodes is acquired by GITT (Fig. 4a), which is utilized to assess the Li$^+$ diffusion coefficient (D$_{Li+}$) with Eq. (5) [41]:

$$D_{Li^+} = \frac{4L^2}{\pi\tau}\left(\frac{\Delta E_S}{\Delta E_\tau}\right)^2 \tag{5}$$

Therein, L represents the Li$^+$ diffusion distance, designating as the thickness of electrode; τ refers to the relaxation time. The calculated D$_{Li+}$ of SnS$_2$/NC at charging state is between 9.92×10^{-10} and 5.28×10^{-9} cm^2/s (Fig. S11a), while SnS$_2$/C ranges from 9.38×10^{-10} to 5.19×10^{-9} cm^2/s at charging state (Fig. S11b). The higher D$_{Li+}$ of SnS$_2$/NC further demonstrates that the N-doping can augment defects in the CM and furnish more active sites for Li$^+$ storage.

To obtain an insight understanding about the fabulous rate capability of SnS$_2$/NC, the kinetic analysis of the electrode was implemented. Fig. 4b and f display the CV profiles of SnS$_2$/NC and SnS$_2$/C at various sweep rates. The capacitive contribution could be quantified by employing Eq. (6) [32,42]:

$$i = av^b \tag{6}$$

Among them, a and b are constants. b = 0.5 and 1 individually reflect a diffusion-controlled and capacitive process. In our cases, as described in Fig. 4c and g, the b values of both electrodes are evaluated as 0.5–1.0, implying a coupled diffusion-controlled and pseudocapacitive process [43,44]. To disentangle the coupled process, the following Eqs. are used [45,46]:

$$i(V) = k_1v + k_2v^{1/2} \tag{7}$$

$$i(V)/v^{1/2} = k_1v^{1/2} + k_2 \tag{8}$$

Herein, the $k_1v^{1/2}$ stands for the diffusion-controlled process and k_2v signifies the capacitive-controlled process. As calculated, the SnS$_2$/NC electrode (Fig. 4d) possesses a higher capacitive contribution of 84.3% than the SnS$_2$/C (83.2%, Fig. 4h) at 1 mV/s. In addition, in contrast to SnS$_2$/C electrode (Fig. 4i), SnS$_2$/NC electrode delivers larger ratios of capacitive contribution (Fig. 4e), which is consistent with its better rate capability. These results suggest that the enhanced capacitive behavior primarily originates from the N-doping, which supplies more active sites for Li storage. Furthermore, the synergistic constructing effect between SnS$_2$ nanosheets and NC can further promote Li$^+$ absorption, leading to the large capacitive behavior.

To obtain a deeper insight into the N-doping influence on the electronic conductivity of SnS$_2$, DFT calculations were implemented. The PDOS of SnS$_2$/C and SnS$_2$/NC are revealed elaborately. Compared with SnS$_2$/C (Fig. 5a), the PDOS value of SnS$_2$/NC around the Fermi level
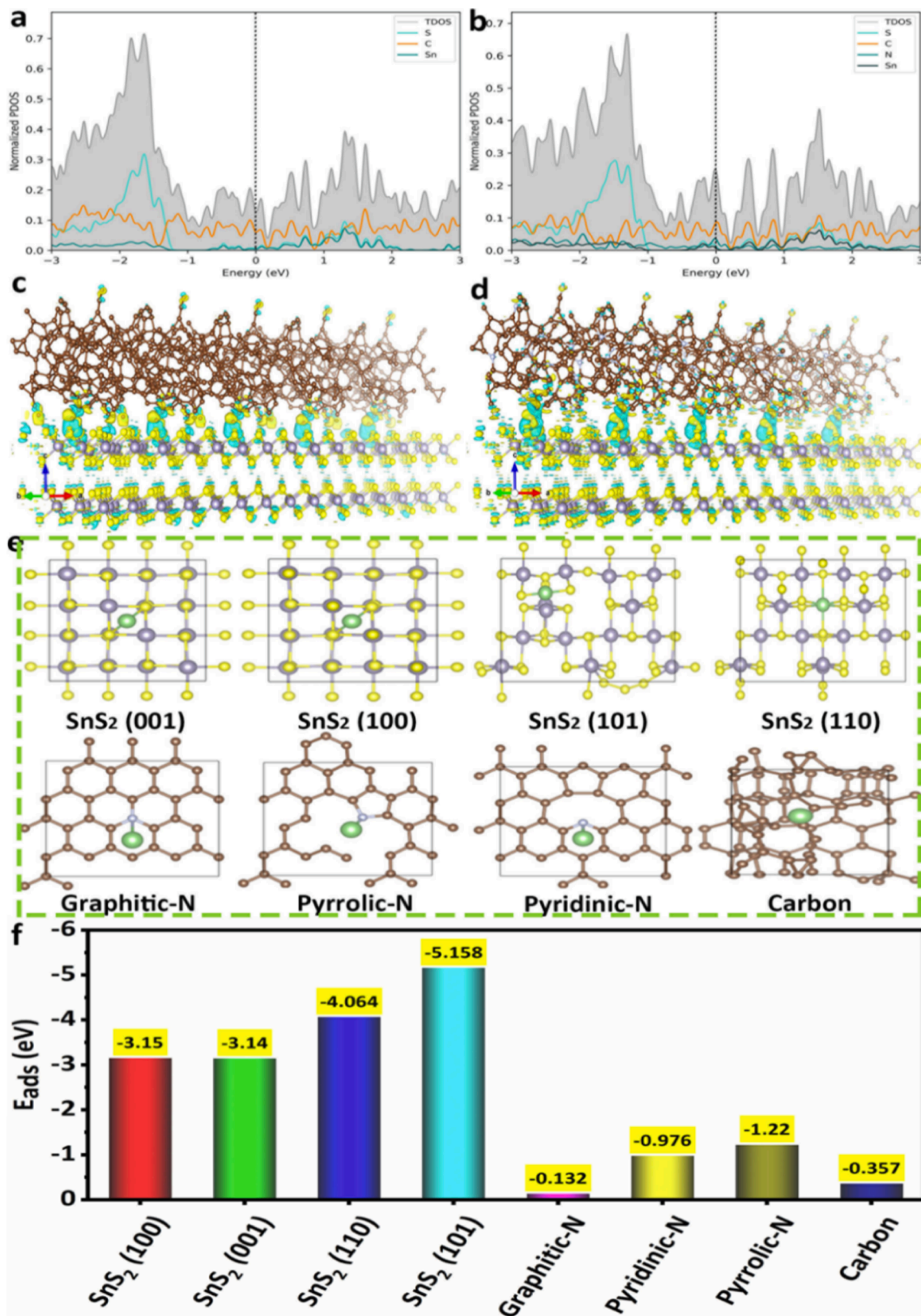
Fig. 5. Partial density of states (PDOS) of (a) SnS$_2$/C and (b) SnS$_2$/NC. Charge density difference of (c) SnS$_2$/C and (d) SnS$_2$/NC. (e) Modeling of SnS$_2$, NC, and C. (f) A survey of the calculated adsorption energies (E$_{ads}$) of Li atom with SnS$_2$, NC, and C.
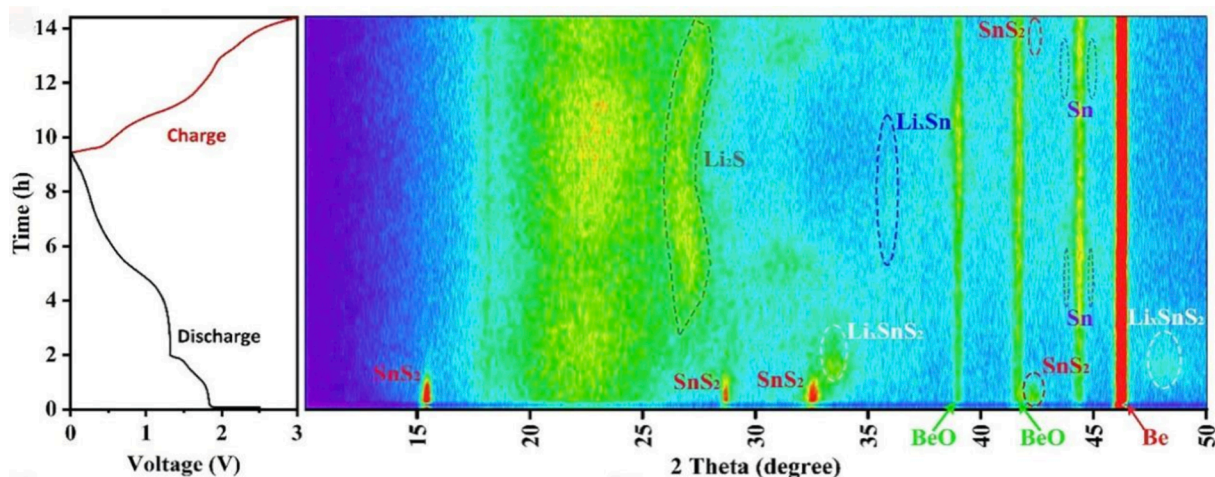
Fig. 6. Contour plots of the in-situ XRD results for SnS$_2$/NC electrode at different charge/discharge (CD) states.

(Fig. 5b) is enhanced significantly, as well as the contribution of the introduced N element to the peak intensity, which suggests that the electronic conductivity and electron transport kinetics after N-doping are superior to those of SnS$_2$/C. Meanwhile, the actual electronic conductivity was assessed via four-point probe. The electronic conductivity of SnS$_2$/NC is calculated as 2.91×10^{-3} S/cm (Fig. S10), higher than SnS$_2$/C (1.05×10^{-3} S/cm), illustrating that N-doping can strengthen the electronic conductivity of SnS$_2$, further supporting the DFT calculations.

In addition, the charge density difference maps of SnS$_2$/NC and SnS$_2$/C are provided in Fig. 5c-d. Relative to the SnS$_2$/C (Fig. 5c), the SnS$_2$/NC exhibits a greater degree of charge transfer (Fig. 5d), indicating powerful electronic interaction at the interface of SnS$_2$/NC, which can efficaciously reinforce the electronic conductivity and ion diffusion kinetics of SnS$_2$/NC because of the promoted charge transport at the interface.

To gain a better understanding of the N-doping influence on the properties of SnS$_2$, the Li-adsorption abilities on various structures were simulated by DFT calculations (Fig. 5e). The computed adsorption energies (E$_{ads}$) between Li atoms and various species within the SnS$_2$/NC host are generalized systematically in Fig. 5f. Specifically, SnS$_2$ (101) displays the highest E$_{ads}$, reflecting boosted Li$^+$ transport kinetics in the (101) plane. In addition, the E$_{ads}$ of Li atom adsorbed on the pure carbon is -0.357 eV. After introducing different N-doping sites, the E$_{ads}$ values are calculated as -0.132 eV (Graphitic-N), -0.976 eV (Pyridinic-N), and -1.22 eV (Pyrrolic-N), separately. The higher E$_{ads}$ of Pyridinic-N and Pyrrolic-N manifest the more powerful Li$^+$ adsorption ability. As a result, it is theoretically vindicated the improved Li$^+$ storage capabilities after N-doping, such as eminent rate performance and capacitive behavior.

To clearly expound the Li$^+$ storage mechanisms of SnS$_2$/NC at different charge/discharge (CD) states, in-situ XRD analysis for the initial cycle was performed between 0.01 and 3.0 V (Fig. 6 and Fig. S12). The peaks at 39.0°, 41.6°, 44.4°, and 46.3° are designated as BeO and Be. During the initial discharging, the peaks at 15.4, 28.6, 32.1, and 41.9° are associated with SnS$_2$. With the discharge process proceeding, the intensities of SnS$_2$ peaks gradually turn weaker and vanish. Simultaneously, two new peaks emerge at 33.4° and 48.2°, relevant to the Li$^+$ embedding into SnS$_2$ to form Li$_x$SnS$_2$. When discharged to 1.22 V, the diffraction peaks induced by metallic Sn are observed at 43.9° and 45.0°, and a new peak generates at 27° originating from the byproduct of Li$_2$S, suggesting the conversion of Li$_x$SnS$_2$ into Sn and Li$_2$S. With further discharging, the peaks of the Sn disappear entirely, and the peaks of Li$_x$Sn appear at 22.3 and 35.9°, which demonstrates the conversion from Sn to Li$_x$Sn alloys. During the charge processes, the peak signals of Li$_x$Sn gradually fade away at 0.80 V, together with the formation of metallic

Sn, indicating the dealloying process of Li$_x$Sn alloys. With the electrode continuing charging, the peaks of Sn entirely disappear, whereas the peak of Li$_x$SnS$_2$ is detected, implying the reverse conversion reaction between Sn and Li$_2$S. After charging to 3 V, the diffraction peak of SnS$_2$ reoccurs at 41.9°, which signifies the reversible emergence of SnS$_2$. There are no strong diffraction peaks observed during cycling, indicative of the poor crystallinity of SnS$_2$. The phenomenon was found in the SnS$_2$ anode previously reported [34,45,47-49].

To recap, the Li$^+$ storage mechanisms of SnS$_2$/NC electrode at different CD states can be described in (9)-(14):

Intercalation:

$$SnS_2 + xLi^+ + xe^- \rightarrow Li_xSnS_2 \tag{9}$$

Conversion:

$$Li_xSnS_2 + (4-x)Li^+ + (4-x)e^- \rightarrow Sn + 2Li_2S \tag{10}$$

Alloying:

$$Sn + xLi^+ + xe^- \rightarrow Li_xSn \tag{11}$$

Dealloying:

$$Li_xSn \rightarrow Sn + xLi^+ + xe^- \tag{12}$$

Reverse conversion:

$$Sn + 2Li_2S \rightarrow Li_xSnS_2 + (4-x)Li^+ + (4-x)e^- \tag{13}$$

Deintercalation:

$$Li_xSnS_2 \rightarrow SnS_2 + xLi^+ + xe^- \tag{14}$$
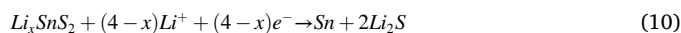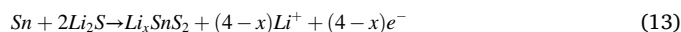
To reveal the process of the conversion evolution of the SnS$_2$/NC electrode, the ex-situ XPS was performed at diverse CD states (Fig. 7). The initial CD profiles are provided in Fig. 7a. After discharged to 1.9 V, two distinct peaks at 495 and 486.6 eV belong to Sn 3d$_{3/2}$ and Sn 3d$_{5/2}$ (Fig. 7b), which are the same as the Sn 3d of fresh SnS$_2$/NC, suggesting that SnS$_2$ still exists. When discharged to 1.52 (Fig. 7c) and 1.2 V (Fig. 7d), each peak can be deconvoluted as two peaks originating from Sn^{4+} (495 and 486.7 eV) and Sn^0 (494.4 and 486 eV), illustrating the coexistence of Sn^{4+} and Sn^0. Specifically, the two peak intensities of Sn^0 (Fig. 7d) are stronger than those of Fig. 7c, while the peak intensities of Sn^{4+} gradually become weaker, indicating the gradual conversion reaction of SnS$_2$ to Sn. After discharging to 0.65 V (Fig. 7e), the two peaks of Sn^{4+} vanish utterly, manifesting that SnS$_2$ has been thoroughly converted to Sn. With further discharge to 0.01 V (Fig. 7f), the Sn^0 peaks still exist. Meanwhile, the new peaks at 492.8 and 482.9 eV are connected with the Li-Sn bond in Li$_x$Sn alloy [17]. After charged to 0.8 V, the electrode merely shows the Sn^0 peaks (Fig. 7g), suggesting the
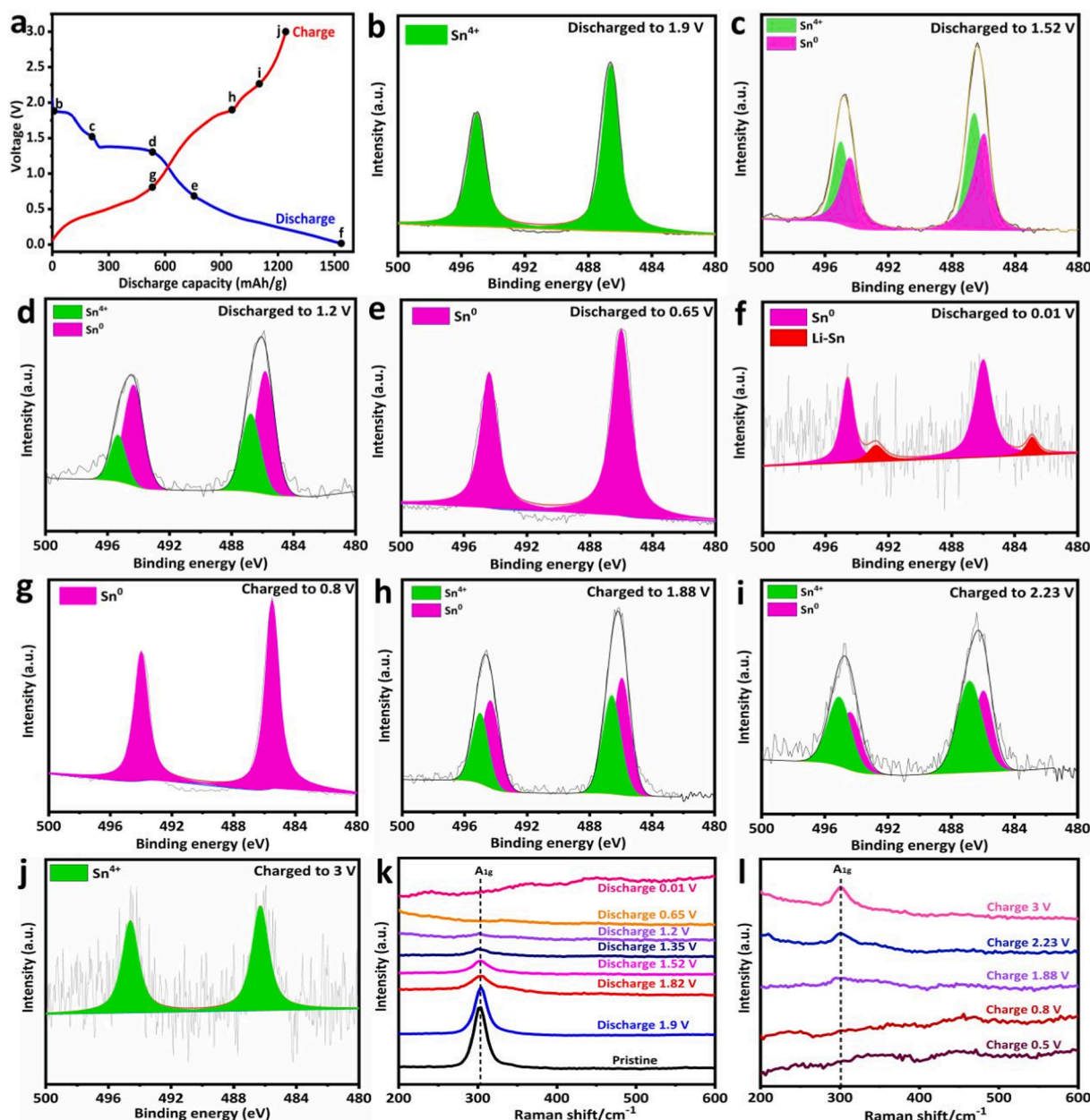
Fig. 7. Ex-situ Sn 3d XPS spectra of SnS_2/NC at various CD states (b-j). (a) The initial CD profiles of SnS_2/NC at 100 mA/g. After discharged to (b) 1.9 V, (c) 1.52 V, (d) 1.2 V, (e) 0.65 V, (f) 0.01 V. After charged to (g) 0.8 V, (h) 1.88 V, (i) 2.23 V and (j) 3 V. Ex-situ Raman spectra of SnS_2/NC at diverse (k) discharge and (l) charge voltages.

dealloying reaction of Li_xSn to form Sn. When charged to 1.88 (Fig. 7h) and 2.23 V (Fig. 7i), the two peaks assigned to the Sn^{4+} signal emerge gradually, which means the gradual conversion of Sn to SnS_2. After charging to 3 V, two significant Sn^{4+} signal peaks can be detected (Fig. 7j), implying the formation of SnS_2. These results well confirm the process of conversion evolution as plotted in Eqs. (2–4). In addition, the S 2p spectrum of SnS_2/NC electrode discharging to 0.01 V displays three weak peaks centered at 160.5, 161.9, and 162.7 eV (Fig. S13a), belonging to the Li_2S, terminal S (S_T) of partial polysulfide species (Li_2S_2 or Li_2S_4), as well as Li_2S_3, respectively [17,50]. The peaks about 168.6 and 170 eV may be because of the side oxidation of S^{2-} [51]. After charging to 3 V, the S 2p spectrum (Fig. S13b) outlines three peaks including the S_T (161.8 eV), bridging S (S_B) in polysulfides Li_2S_n (n > 4) (163.3 eV), and elemental S (S_8, 164.4 eV) [50,52,53], while the peak around 168.6 eV still remains. The above outcomes prove the reversibility of conversion and alloying reactions. Besides, the existence of

intermediate polysulfides means that, apart from the mentioned conversion and alloying reaction, mutual multi-step transformation from Li_2S into low- and high-ordered polysulfides, as well as elemental S [17,52,53], take place during lithiation/delithiation process. This phenomenon was analogous to that previously reported in $WS_2/g-C_3N_4$ composite [54]. Fig. S13c also gives the XPS spectra of Li 1s after discharging to 0.01 V. Two obvious peaks at 54.5 and 55 eV are derived from Li-N and Li-S bonds [55], while the additional peak at 55.6 eV represents Li-Sn bond [56], which further reveals that the SnS_2 is converted to Li_2S and Li_xSn alloy at this discharge stage, conforming with the reaction Eqs. (2–4) mentioned above. Additionally, Sn 3d spectrum only shows the presence of Sn $3d_{3/2}$ and Sn $3d_{5/2}$ after 50 cycles (Fig. S13d), matching well with the Sn 3d spectrum of fresh SnS_2/NC, which substantiates the reaction stability of SnS_2/NC electrode.

Additionally, the evolution mechanism of the SnS_2/NC electrode was further probed via ex-situ Raman spectra, as plotted in Fig. 7k and l. The
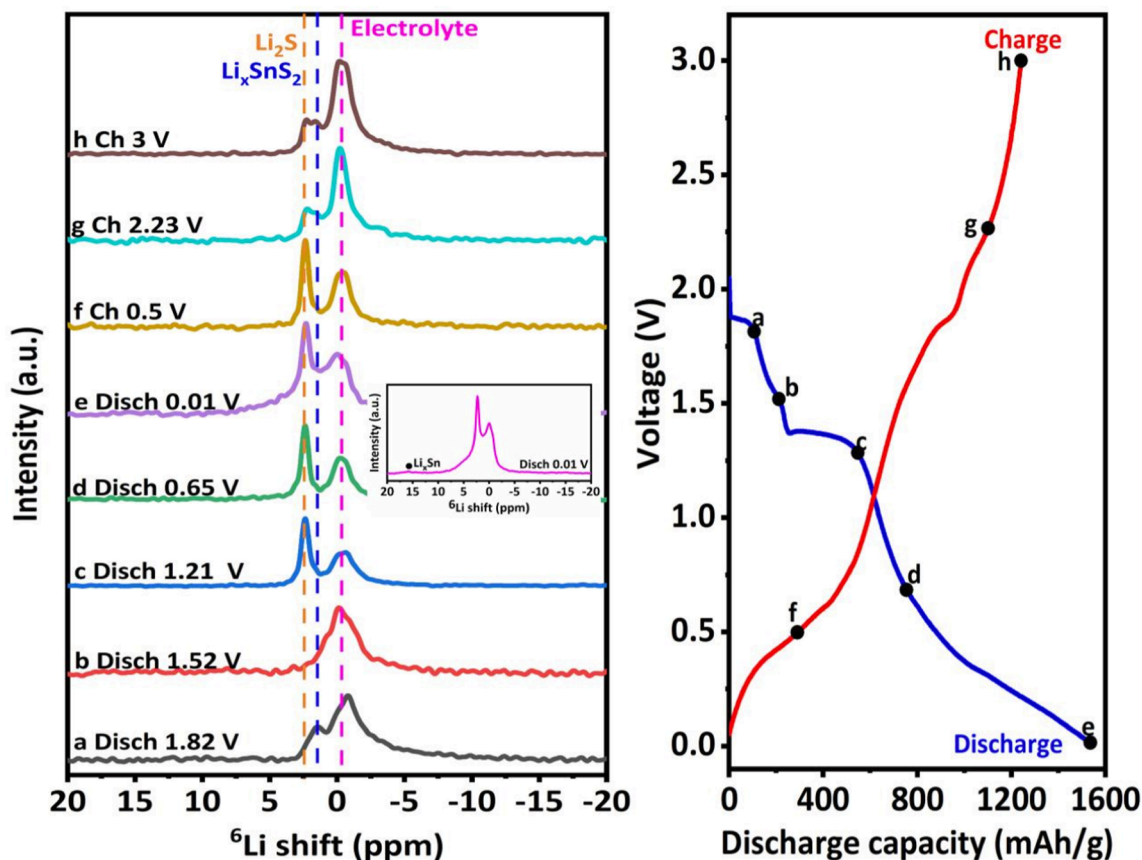
Fig. 8. Ex-situ solid state ^{6}Li MAS NMR spectra for SnS$_2$/NC electrode at various CD states. The initial CD curve is plotted on the right.

A$_{1g}$ mode of SnS$_2$ ($\approx$307 cm^{-1}) can be observed in the pristine electrode. With the intercalation of Li$^+$, the intensity of the A$_{1g}$ mode peak decreases gradually and almost fades away when discharging to 0.65 V, which is relevant to the conversion of SnS$_2$. Upon charging, the A$_{1g}$ mode peak of SnS$_2$ appears at 1.88 V, and the A$_{1g}$ mode peak can be clearly detected at 2.23 V and 3 V, manifesting the reversible formation of SnS$_2$.

Nuclear magnetic resonance (NMR) spectroscopy has been testified as an effective tool to determine the local structure modification [57,58]. Here, solid-state ^{6}Li and ^{7}Li MAS NMR spectra of SnS$_2$/NC electrode were collected and analyzed at different CD states during the first cycling. As plotted in Fig. S14a, all ^{7}Li spectra display an isotropic signal located near 0 ppm with multiple orders spinning sidebands (SSBs) up to 600 ppm. Two or three components (overlapped peaks) are observed for all cycled electrodes. Therefore, we turn to ^{6}Li NMR spectra with better spectral resolution due to its smaller quadrupole moment compared to that of ^{7}Li. After discharging to 1.82 V (Fig. 8), the electrode shows a peak at −0.3 ppm, which is related to the residual electrolyte (1 M LiPF$_6$) [59]. Another peak at 1.4 ppm originates from Li$_x$SnS$_2$. With further discharging to 1.21 V, a new peak appears at ~2.35 ppm, indicating the formation of Li$_2$S [60]. Upon deeply discharged to 0.01 V, a weak ^{6}Li signal at around 15.8 ppm could be connected with the formation of Li$_x$Sn [61-63]. A reversible evolution trend is observed for the subsequent charge process. Additionally, a similar evolution is detected for ^{7}Li NMR spectra. As shown in Fig. S14, for the fully discharged sample at 0.01 V (Fig. S14c-d), three ^{7}Li signals at around 41.2 ppm, 30.5 ppm, and 15.8 ppm are ascribed to the generation of Li$_x$Sn [61-63], which is not clearly detected in ^{6}Li NMR spectrum because of low natural abundance of ^{6}Li. In conclusion, the Li$^+$ is first embedded into the SnS$_2$ to form Li$_x$SnS$_2$ upon discharge. With the embedding of Li$^+$, the Li$_x$SnS$_2$ converts to the Li$_2$S. When fully discharged, Li$_x$Sn alloy is further formed.

To prove the feasibility of SnS$_2$/NC anode for actual implementation, a full cell was assembled employing LiCoO$_2$ as cathode (Fig. 9a). As plotted in Fig. 9b-c, the SnS$_2$/NC||LiCoO$_2$ full cell achieves initial charge/discharge capacities of 998.4/642.3 mAh/g (based on the mass of anode) at 200 mA/g, with an ICE of 64.3%. After 90 cycles, there is 467.9 mAh/g capacity maintained, showing a capacity deterioration of solely 0.3% per cycle and possessing a CE of 97.9%. More importantly, by connecting the full cell, commercial LED equipment can be lightened (Fig. 9d-e). The above results further testify the actual application perspective of SnS$_2$/NC anode in LIBs.

4. Conclusions

In summary, we have successfully devised SnS$_2$/NC composite via a simple and green strategy and systematically studied its evolution mechanism and electronic conductivity of nitrogen-doped carbon to SnS$_2$. DFT calculations demonstrate that N doping increases the electronic conductivity, and also certify that the pyridinic-N and pyrrolic-N doped carbon structures are instrumental in the adsorbing Li$^+$. These superiorities bestow the SnS$_2$/NC composite with an impressive discharge capacity (863.9 mAh/g at 100 mA/g over 100 cycles). Additionally, the assembled SnS$_2$/NC||LiCoO$_2$ full cell possesses a capacity attenuation of solely 0.3% per cycle after 90 cycles, which can light up LED equipment. In-situ XRD, ex-situ XPS, and NMR spectra unravel the sequential evolution mechanism of SnS$_2$ upon lithiation, involving intercalation ($SnS_2 + xLi^+ + xe^- \rightarrow Li_xSnS_2$), conversion ($Li_xSnS_2 + (4-x)Li^+ + (4-x)e^- \rightarrow Sn + 2Li_2S$) and alloying ($Sn + xLi^+ + xe^- \rightarrow Li_xSn$) reactions. Ex-situ Raman unveils the reversible evolution of SnS$_2$. Meaningfully, these findings could provide significant reference and guideline for the evolution mechanism of other metal sulfides materials.
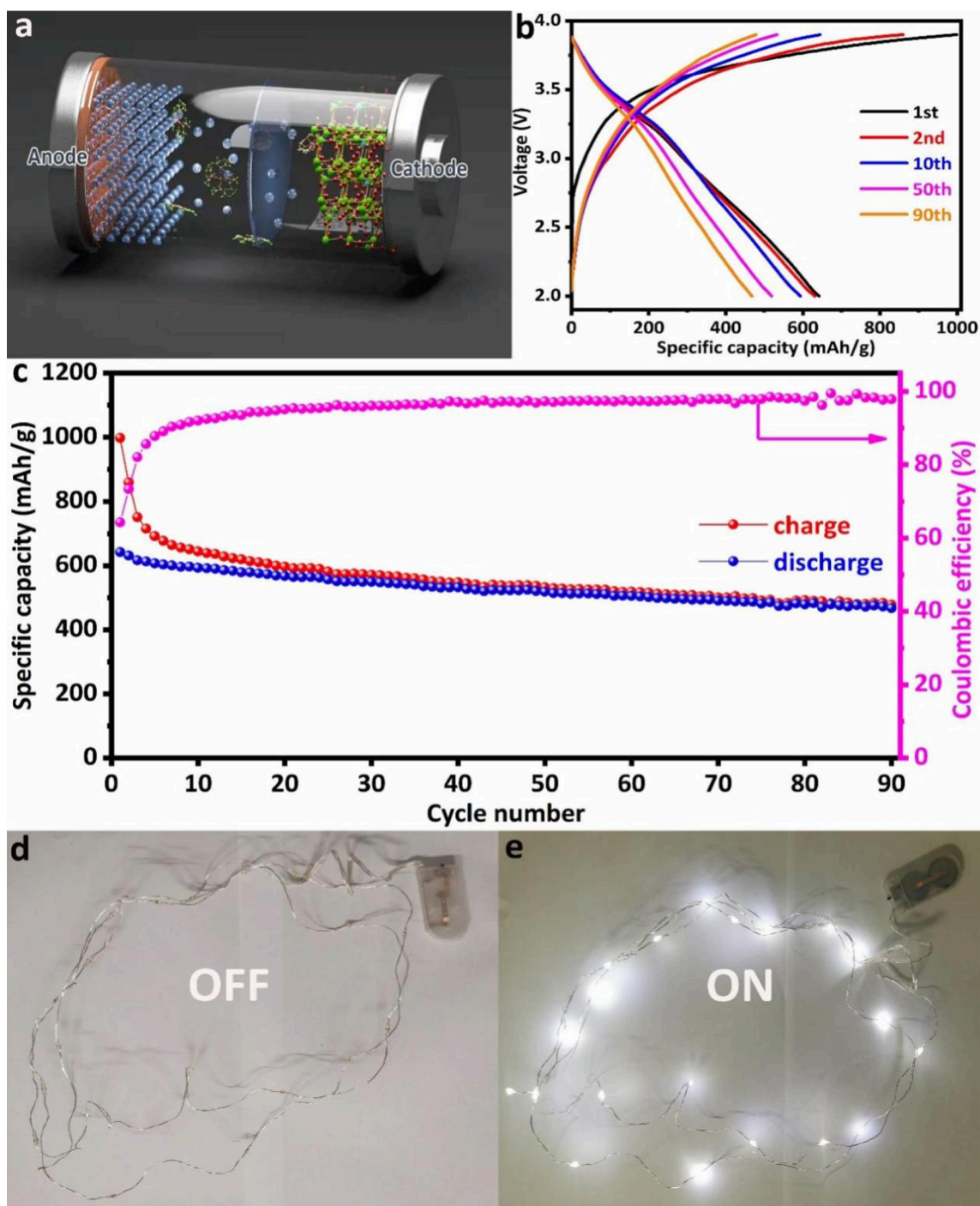
Fig. 9. (a) Schematic illustration of $SnS_2/NC||LiCoO_2$ full cell configuration. (b) GCD profiles and (c) cycling property at 200 mA/g. (d-e) Digital photo of LED equipment lit by $SnS_2/NC||LiCoO_2$ full cell.

CRediT authorship contribution statement

Kun Liu: Conceptualization, Investigation, Methodology, Writing – original draft. **Jia-ao Wang:** Writing – review & editing, Formal analysis. **Chenjie Lou:** Software. **Ziru Zhou:** Investigation. **Ning Zhang:** Formal analysis. **Yingtao Yu:** Data curation. **Qingxiao Zhang:** Writing – review & editing, Funding acquisition. **Graeme Henkelman:** Data curation. **Mingxue Tang:** Data curation. **Juncai Sun:** Supervision, Writing – review & editing, Funding acquisition.

Declaration of Competing Interest

The authors declare that they have no known competing financial interests or personal relationships that could have appeared to influence the work reported in this paper.

Data availability

Data will be made available on request.

Acknowledgements

Appendix A. Supplementary material

Supplementary data to this article can be found online at https://doi.org/10.1016/j.apsusc.2023.156673.

References

[1] Z. Yan, Z. Sun, L. Zhao, H. Liu, Z. Guo, Y. Qiu, P. Wang, L. Qian, In-situ induced sulfur vacancy from phosphorus doping in FeS$_2$ microflowers for high-efficiency lithium storage, Mater. Today Nano 20 (2022), 100261.

[2] D.-Y. Shin, J.S. Lee, H.-J. Ahn, Hierarchical porous carbon nanofibers with ultrasmall-sized cobalt disulfide/tungsten disulfide hybrid composites for high-rate lithium storage kinetics, Appl. Surf. Sci. 550 (2021), 149298.

[3] Y.V. Fedoseeva, A.A. Makarova, S.G. Stolyarova, V.E. Arkhipov, E. Rühl, A.V. Okotrub, L.G. Bulusheva, Lithium-induced intralayer rearrangement of molybdenum disulfide: effect of graphene coating, Appl. Surf. Sci. 598 (2022), 153846.

[4] L. Wu, J. Zheng, L. Wang, X. Xiong, Y. Shao, G. Wang, J.H. Wang, S. Zhong, M. Wu, PPy-encapsulated SnS$_2$ nanosheets stabilized by defects on a TiO$_2$ support as a durable anode material for lithium-ion batteries, Angew. Chem. Int. Ed. 58 (2019) 811–815.

[5] Y. Shan, Y. Li, H. Pang, Applications of Tin sulfide-based materials in lithium-ion batteries and sodium-ion batteries, Adv. Funct. Mater. 30 (2020) 2001298.

[6] H. Liu, C. Wei, Z. Ai, M. Li, M. Xu, C. Ma, J. Shi, The positive effect of 3D interpenetrating network porous structure by carbon membranes on alleviating the volume expansion of SnS$_2$ nanosheets for enhancing lithium and sodium storage, Colloid Surf. A-Physicochem. Eng. Asp. 610 (2021), 125937.

[7] J.-G. Wang, H. Sun, H. Liu, D. Jin, R. Zhou, B. Wei, Edge-oriented SnS$_2$ nanosheet arrays on carbon paper as advanced binder-free anodes for Li-ion and Na-ion batteries, J. Mater. Chem. A 5 (2017) 23115–23122.

[8] Y. Cheng, H. Xie, L. Zhou, B. Shi, L. Guo, J. Huang, In-situ liquid-phase transformation of SnS$_2$/CNTs composite from SnO$_2$/CNTs for high performance lithium-ion battery anode, Appl. Surf. Sci. 566 (2021), 150645.

[9] Y. Liu, X.-Y. Yu, Y. Fang, X. Zhu, J. Bao, X. Zhou, X.W. Lou, Confining SnS$_2$ ultrathin nanosheets in hollow carbon nanostructures for efficient capacitive sodium storage, Joule 2 (2018) 725–735.

[10] J. Zheng, X. Xiong, G. Wang, Z. Lin, X. Ou, C. Yang, M. Liu, SnS$_2$ nanoparticles anchored on three-dimensional reduced graphene oxide as a durable anode for sodium ion batteries, Chem. Eng. J. 339 (2018) 78–84.

[11] Y. Shen, S. Deng, P. Liu, Y. Zhang, Y. Li, X. Tong, H. Shen, Q. Liu, G. Pan, L. Zhang, X. Wang, X. Xia, J. Tu, Anchoring SnS$_2$ on TiC/C backbone to promote sodium ion storage by phosphate ion doping, Small 16 (2020) 2004072.

[12] W. Ren, H. Zhang, C. Guan, C. Cheng, SnS$_2$ nanosheets arrays sandwiched by N-doped carbon and TiO2 for high-performance Na-ion storage, Green Energy Environ. 3 (2018) 42–49.

[13] Y. Jiang, Y. Feng, B. Xi, S. Kai, K. Mi, J. Feng, J. Zhang, S. Xiong, Ultrasmall SnS$_2$ nanoparticles anchored on well-distributed nitrogen-doped graphene sheets for Li-ion and Na-ion batteries, J. Mater. Chem. A 4 (2016) 10719–10726.

[14] Y.-Q. Wu, Y.-S. Zhao, W.-J. Meng, Y. Xie, J. Zhang, C.-J. He, D.-L. Zhao, Nanoplates-assembled SnS$_2$ nanoflowers with carbon coating anchored on reduced graphene oxide for high performance Li-ion batteries, Appl. Surf. Sci. 539 (2021), 148283.

[15] P. Wu, N. Du, H. Zhang, J. Liu, L. Chang, L. Wang, D. Yang, J.Z. Jiang, Layer-stacked tin disulfide nanorods in silica nanoreactors with improved lithium storage capabilities, Nanoscale 4 (2012) 4002–4006.

[16] J. Liu, Y. Wen, P.A. van Aken, J. Maier, Y. Yu, In situ reduction and coating of SnS$_2$ nanobelts for free-standing SnS@polypyrrole-nanobelt/carbon-nanotube paper electrodes with superior Li-ion storage, J. Mater. Chem. A 3 (2015) 5259–5265.

[17] H. Tran Huu, H.T.T. Le, T. Huong Nguyen, L. Nguyen Thi, V. Vo, W. Bin Im, Facile synthesis of SnS$_2$@g-C$_3$N$_4$ composites as high performance anodes for lithium ion batteries, Appl. Surf. Sci. 549 (2021) 149312–149324.

[18] J. Li, L. Han, Y. Li, J. Li, G. Zhu, X. Zhang, T. Lu, L. Pan, MXene-decorated SnS$_2$/Sn$_3$S$_4$ hybrid as anode material for high-rate lithium-ion batteries, Chem. Eng. J. 380 (2020) 122590–122598.

[19] J. Liu, Y. Qi, B. Fu, J. Dai, Q. Wang, X. Zhu, X. Shi, Li$^+$ diffusion kinetics of SnS$_2$ nanoflowers enhanced by reduced graphene oxides with excellent electrochemical performance as anode material for lithium-ion batteries, J. Alloys Compd. 794 (2019) 285–293.

[20] H. Yang, Y. Su, L. Ding, J. Lin, T. Zhu, S. Liang, A. Pan, G. Cao, Rational synthesis of SnS$_2$@C hollow microspheres with superior stability for lithium-ion batteries, Sci. China Mater. 60 (2017) 955–962.

[21] K. Liu, H. Zheng, J.-A. Wang, Y. Zhou, N. Zhang, Y. Du, J. Man, G. Henkelman, J. Sun, Green self-derived templating preparation of nitrogen, sulfur co-doped porous carbon/tin composites with synergistic effect towards high-performance lithium-ion batteries, Appl. Surf. Sci. 580 (2021), 152319.

[22] Y. Wang, Y. Zhang, J. Shi, X. Kong, X. Cao, S. Liang, G. Cao, A. Pan, Tin sulfide nanoparticles embedded in sulfur and nitrogen dual-doped mesoporous carbon fibers as high-performance anodes with battery-capacitive sodium storage, Energy Storage Mater. 18 (2019) 366–374.

[23] K. Liu, J.-A. Wang, H. Zheng, X. Sun, Z. Yang, J. Man, X. Wang, J. Sun, Direct synthesis of tin spheres/nitrogen-doped porous carbon composite by self-formed template method for enhanced lithium storage, J. Mater. Sci. Technol. 104 (2022) 88–97.

[24] Q. Hu, B. Wang, C. Hu, Y. Hu, J. Lu, H. Dong, C. Wu, S. Chang, L. Zhang, Enhanced electrochemical performance by in situ phase transition from SnS$_2$ nanoparticles to SnS nanorods in N-doped hierarchical porous carbon as anodes for lithium-ion batteries, ACS Appl. Energ. Mater. 3 (2020) 11318–11325.

[25] D. Li, X. Ren, Q. Ai, Q. Sun, L. Zhu, Y. Liu, Z. Liang, R. Peng, P. Si, J. Lou, J. Feng, L. Ci, Facile fabrication of nitrogen-doped porous carbon as superior anode material for potassium-ion batteries, Adv. Energy Mater. 8 (2018) 1802386.

[26] H. Li, B. Zhang, X. Wang, J. Zhang, T. An, Z. Ding, W. Yu, H. Tong, Heterostructured SnO$_2$-SnS$_2$@C embedded in nitrogen-doped graphene as a robust anode material for lithium-ion batteries, Front. Chem. 7 (2019) 339.

[27] S. Huang, M. Wang, P. Jia, B. Wang, J. Zhang, Y. Zhao, N-graphene motivated SnO$_2$@SnS$_2$ heterostructure quantum dots for high performance lithium/sodium storage, Energy Storage Mater. 20 (2019) 225–233.

[28] Q. Hu, B. Wang, S. Chang, C. Yang, Y. Hu, S. Cao, J. Lu, L. Zhang, H. Ye, Effects of annealing temperature on electrochemical performance of SnS$_x$ embedded in hierarchical porous carbon with N-carbon coating by in-situ structural phase transformation as anodes for lithium ion batteries, J. Mater. Sci. Technol. 84 (2021) 191–199.

[29] L. Huang, T. Guan, H. Su, Y. Zhong, F. Cao, Y. Zhang, X. Xia, X. Wang, N. Bao, J. Tu, Synergistic interfacial bonding in reduced graphene oxide fiber cathodes containing Polypyrrole@sulfur nanospheres for flexible energy storage, Angew. Chem. Int. Ed. 61 (2022) e202212151.

[30] A.v.W. Cresce, K. Xu, Aqueous lithium-ion batteries, Carbon Energy, 3 (2021) 721–751.

[31] J.G. Wang, H. Sun, H. Liu, D. Jin, X. Liu, X. Li, F. Kang, Triaxial nanocables of conducting polypyrrole@SnS$_2$@carbon nanofiber enabling significantly enhanced li-ion storage, ACS Appl. Mater. Interfaces 10 (2018) 13581–13587.

[32] Y. Hao, S. Wang, Y. Shao, Y. Wu, S. Miao, High-energy density li-ion capacitor with layered SnS$_2$/reduced graphene oxide anode and BCN nanosheet cathode, Adv. Energy Mater. 10 (2019) 1902836.

[33] Y. Jiang, M. Wei, J. Feng, Y. Ma, S. Xiong, Enhancing the cycling stability of Na-ion batteries by bonding SnS$_2$ ultrafine nanocrystals on amino-functionalized graphene hybrid nanosheets, Energy Environ. Sci. 9 (2016) 1430–1438.

[34] Q. Sun, D. Li, L. Dai, Z. Liang, L. Ci, Structural engineering of SnS$_2$ encapsulated in carbon nanoboxes for high-performance sodium/potassium-ion batteries anodes, Small 16 (2020) 2005023.

[35] Y. Wang, J. Zhou, J. Wu, F. Chen, P. Li, N. Han, W. Huang, Y. Liu, H. Ye, F. Zhao, Y. Li, Engineering SnS$_2$ nanosheet assemblies for enhanced electrochemical lithium and sodium ion storage, J. Mater. Chem. A 5 (2017) 25618–25624.

[36] L. Wang, J. Yuan, Q. Zhao, Z. Wang, Y. Zhu, X. Ma, C. Cao, Supported SnS$_2$ nanosheet array as binder-free anode for sodium ion batteries, Electrochim. Acta 308 (2019) 174–184.

[37] X. Lu, D. Liu, T. Han, M. Zhu, S.O. Ryu, J. Huang, A facile synthesis of sandwich-structured SnS$_2$@reduced graphene oxide with high performance for lithium-ion battery anode, J. Alloys Compd. 765 (2018) 1061–1071.

[38] P. Zheng, Z. Dai, Y. Zhang, K.N. Dinh, Y. Zheng, H. Fan, J. Yang, R. Dangol, B. Li, Y. Zong, Q. Yan, X. Liu, Scalable synthesis of SnS$_2$/S-doped graphene composites for superior Li/Na-ion batteries, Nanoscale 9 (2017) 14820–14825.

[39] X. Xiao, F. Zhao, J. Liu, Z. Wang, Q. Sui, M. Tan, Synthesis of hexahedron SnS$_2$/C derived from tin metal-organic frameworks (Sn-MOF) as a promising anode for lithium-ion batteries, Mater. Lett. 296 (2021) 129877–129880.

[40] Y. Zuo, X. Xu, C. Zhang, J. Li, R. Du, X. Wang, X. Han, J. Arbiol, J. Llorca, J. Liu, A. Cabot, SnS$_2$/g-C$_3$N$_4$/graphite nanocomposites as durable lithium-ion battery anode with high pseudocapacitance contribution, Electrochim. Acta 349 (2020) 136369–136379.

[41] X. Chen, H. Jiang, Y. Pei, Y. Chen, Y. Zeng, H. Guo, Binder-free ultrathin SnS$_2$ with superior reversibility of conversion reaction for high-rate lithium ion batteries, J. Alloys Compd. 873 (2021) 159623–159632.

[42] K. Liu, J.-A. Wang, H. Zheng, S. Guo, X. Wang, J. Man, X. Wang, J. Sun, A sustainable strategy for fabricating porous carbon supported Sn submicron spheres by self-generated Na$_2$CO$_3$ as templates for lithium-ion battery anode, Green Chem. 23 (2021) 6490.

[43] J. Zhang, D. Cao, Y. Wu, X. Cheng, W. Kang, J. Xu, Phase transformation and sulfur vacancy modulation of 2D layered tin sulfide nanoplates as highly durable anodes for pseudocapacitive lithium storage, Chem. Eng. J. 392 (2020), 123722.

[44] S. Niu, Z. Wang, M. Yu, M. Yu, L. Xiu, S. Wang, X. Wu, Q. Qiu, MXene-based electrode with enhanced pseudocapacitance and volumetric capacity for power-type and ultra-long life lithium storage, ACS Nano 12 (2018) 3928–3937.

[45] J. Xie, Y. Zhu, N. Zhuang, X. Li, X. Yuan, J. Li, G. Hong, W. Mai, High-concentration ether-based electrolyte boosts the electrochemical performance of SnS$_2$–reduced graphene oxide for K-ion batteries, J. Mater. Chem. A 7 (2019) 19332–19341.

[46] T. Zhang, C. Li, F. Wang, A. Noori, M.F. Mousavi, X. Xia, Y. Zhang, Recent advances in carbon anodes for sodium-ion batteries, Chem. Rec. 22 (2022) e202200083.

[47] C. Ma, J. Xu, J. Alvarado, B. Qu, J. Somerville, J.Y. Lee, Y.S. Meng, Investigating the energy storage mechanism of SnS$_2$-rGO composite anode for advanced Na-Ion batteries, Chem. Mater. 27 (2015) 5633–5640.

[48] X. Shi, Z. Yang, Y. Liu, Y. Tang, Y. Liu, S. Gao, Y. Yang, X. Chen, Y. Zhong, Z. Wu, X. Guo, B. Zhong, Three-dimensional SnS_2 nanoarrays with enhanced lithium-ion storage properties, ChemElectroChem 7 (2020) 4484–4491.

[49] Z. Kong, M. Huang, Z. Liang, H. Tu, K. Zhang, Y. Shao, Y. Wu, X. Hao, Phosphorus doping induced the co-construction of sulfur vacancies and heterojunctions in tin disulfide as a durable anode for lithium/sodium-ion batteries, Inorg. Chem. Front. 9 (2022) 902.

[50] G. Zhang, Z.-W. Zhang, H.-J. Peng, J.-Q. Huang, Q. Zhang, A toolbox for lithium-sulfur battery research: methods and protocols, Small Methods 1 (2017) 1700134.

[51] Y. Hu, B. Luo, D. Ye, X. Zhu, M. Lyu, L. Wang, An innovative freeze-dried reduced graphene oxide supported SnS_2 cathode active material for aluminum-ion batteries, Adv. Mater. 29 (2017) 1606132.

[52] C. Zu, Y. Fu, A. Manthiram, Highly reversible Li/dissolved polysulfide batteries with binder-free carbon nanofiber electrodes, J. Mater. Chem. A 1 (2013) 10362.

[53] M.J. Lacey, A. Yalamanchili, J. Maibach, C. Tengstedt, K. Edström, D. Brandell, The Li–S battery: an investigation of redox shuttle and self-discharge behaviour with $LiNO_3$-containing electrolytes, RSC Adv. 6 (2016) 3632–3641.

[54] H.T. Huu, H.T.T. Le, V.P. Nguyen, T.T. Huong Nguyen, T.X. Dieu Nguyen, V. T. Nguyen, S.-J. Kim, V. Vo, Facile one-step synthesis of g–C_3N_4–supported WS_2 with enhanced lithium storage properties, Electrochim. Acta 341 (2020) 136010–136025.

[55] J. Xu, F. Yu, J. Hua, W. Tang, C. Yang, S. Hu, S. Zhao, X. Zhang, Z. Xin, D. Niu, Donor dominated triazine-based microporous polymer as a polysulfide immobilizer and catalyst for high-performance lithium-sulfur batteries, Chem. Eng. J. 392 (2020) 123694–123704.

[56] M. Wu, J. Jin, Z. Wen, Influence of a surface modified Li anode on the electrochemical performance of Li–S batteries, RSC Adv. 6 (2016) 40270–40276.

[57] J. Liu, C. Lou, J. Fu, X. Sun, J. Hou, J. Ma, Y. Chen, X. Gao, L. Xu, Q. Wei, M. Tang, Multiple transition metals modulated hierarchical networks for high performance of metal-ion batteries, J. Energy Chem. 70 (2022) 604–613.

[58] J. Liu, Y. Gao, C. Lou, Y. Chen, X. Gao, L. Xu, Q. Wei, G. Bai, G. Liu, M. Tang, Regulating hybrid anodes for efficient Li^+/Na^+ storage, ACS Mater. Lett. 4 (2022) 1411–1421.

[59] V. Kumar, R.R. Reddy, B.V.N. Phani Kumar, C.V. Avadhani, S. Ganapathy, N. Chandrakumar, S. Sivaram, Lithium speciation in the $LiPF_6$/PC electrolyte studied by two dimensional heteronuclear overhauser enhancement and pulse-field gradient diffusometry NMR, J. Phys. Chem. C. 123 (2019) 9661–9672.

[60] K.A. See, M. Leskes, J.M. Griffin, S. Britto, P.D. Matthews, A. Emly, A. Van der Ven, D.S. Wright, A.J. Morris, C.P. Grey, R. Seshadri, Ab initio structure search and in situ ^7Li NMR studies of discharge products in the Li-S battery system, J. Am. Chem. Soc. 136 (2014) 16368–16377.

[61] A. Ruderman, S. Smrekar, M.V. Bracamonte, E.N. Primo, G.L. Luque, J. Thomas, E. Leiva, G.A. Monti, D.E. Barraco, F.V. Chávez, Unveiling the stability of Sn/Si/graphite composites for Li-ion storage by physical, electrochemical and computational tools, Phys. Chem. Chem. Phys. 23 (2021) 3281–3289.

[62] E. Bekaert, F. Robert, P.E. Lippens, M. Ménétrier, ^7Li NMR Knight shifts in Li-Sn compounds: MAS NMR measurements and correlation with DFT calculations, J. Phys. Chem. C 114 (2010) 6749–6754.

[63] J.E. Frerichs, M. Ruttert, S. Böckmann, M. Winter, T. Placke, M.R. Hansen, Identification of Li_xSn phase transitions during lithiation of tin nanoparticle-based negative electrodes from ex situ ^{119}Sn MAS NMR and operando ^7Li NMR and XRD, ACS Appl. Energy Mater. 4 (2021) 7278–7287.